

Pintle Injector Spray Study via Physics-Based Spray Model and Generative Adversarial Networks

Original

Pintle Injector Spray Study via Physics-Based Spray Model and Generative Adversarial Networks / Stumpo, Leonardo; Ferrero, Andrea; Martelli, Emanuele; Masseni, Filippo; Pastrone, Dario. - (2025). (EUCASS 2025 Rome (ITA) 30 June - 4 July 2025).

Availability:

This version is available at: 11583/3003216 since: 2025-09-20T09:03:22Z

Publisher:

EUCASS

Published

DOI:

Terms of use:

This article is made available under terms and conditions as specified in the corresponding bibliographic description in the repository

Publisher copyright

(Article begins on next page)

Pintle Injector Spray Study via Physics-Based Spray Model and Generative Adversarial Networks

Leonardo Stumpo*[†], Andrea Ferrero*, Emanuele Martelli*, Filippo Masseni* and Dario Pastrone*

*Dipartimento di Ingegneria Meccanica e Aerospaziale, Politecnico di Torino

Corso degli Abruzzi 24, 10129, Turin, Italy

leonardo.stumpo@polito.it · andrea_ferrero@polito.it · emanuele.martelli@polito.it

filippo.masseni@polito.it · dario.pastrone@polito.it

[†]Corresponding author

Abstract

Pintle injectors are increasingly used in liquid rocket engines due to their favorable combustion stability and thrust modulation capabilities. This study presents a multi-stage numerical investigation of spray formation in gas-liquid discrete orifice pintle injectors, aimed at enabling high-fidelity yet computationally efficient simulations. A physics-based modification of the plain orifice atomizer model is proposed to characterize droplet velocity, angle, and size distributions at the injector exit, forming the basis for a Lagrangian spray injection model. Validation through CFD simulations in Ansys Fluent confirms the model's consistency with experimental spray morphology and angle, using a Rosin-Rammler droplet distribution and a breakup model suited for subsonic crossflow conditions. The validated simulation data are further used to train a Physics-Informed Generative Adversarial Network (GAN) that integrates a spray angle evaluator as a physical loss function. The resulting lightweight GAN model shows promising accuracy in generating instantaneous flowfields while maintaining low computational cost, demonstrating the viability of combining physics-driven modeling with data-driven generative techniques for pintle injector flowfield prediction.

1. Introduction

Pintle injectors have seen significant development in the field of rocket propulsion due to their ease of thrust control and inherent combustion stability compared to other types of injectors^[1]. The investigation of the spray flowfield is crucial for the understanding of key-elements for liquid rocket engines combustion chamber performances, such as combustion efficiency, combustion stability, and overall heat flux to the wall^{[2],[3],[4]}. However, the flowfield is in general complex because of the liquid jet breakup and its interaction with the gas crossflow. The study using Computational Fluid Dynamics (CFD) provides accurate information without the need for physical experiments. The main approaches used are the Volume-of-Fluid methods^{[5],[6]} and Lagrangian models^[7]. On one hand, VOF offer an accurate description of the primary breakup but come with a very high computational cost due to the required mesh refinement for tracking the liquid interface. On the other hand, in the Lagrangian models individual particles and their evolution are tracked at a reduced computational cost. To develop an effective Lagrangian model, however, precise modeling of the droplet distribution in terms of velocity, angle, and size near the injector exit is required.

The first objective of this work is to develop a physics-based model for describing the spray characteristics at the exit of gas-liquid pintle injectors. In order to do this, a plain orifice atomizer model is proposed for the discrete orifices-type pintle injector.

The second step is the validation of the proposed model using the CFD software Ansys Fluent. The goal is to verify whether combining the atomizer model, which gives a Rosin-Rammler distribution at the injector exit, with a suitable breakup model based on the physics of liquid injection in subsonic crossflows results in a spray evolution consistent with experimental data in terms of shape and spray angle.

Finally, the database created using the simulations is used to train a Physics-Informed Generative Adversarial Networks (GANs) for the generation of instantaneous flowfields of discrete orifices gas-liquid pintle injectors. In the literature, GANs have already been used for this purpose by Haidn et al.^[8], achieving improvements in training speed and the quality of the generated fields when combined with physical evaluators on the expected spray angle. The physical evaluator is used in both the structure of the Generator and in the adversarial training as a physical loss. This work focuses on training GANs to generate instantaneous fields under operating conditions already present in the

PINTLE INJECTOR SPRAY STUDY

dataset. While this serves as a first step, the long-term objective is to enable predictive generation under previously unseen conditions.

2. Pintle injector generalities

The pintle injector, commonly employed in liquid rocket engines, features a central post with radial discharge discrete orifices or continuous gap^[9]. One propellant exits radially through these ports, while the other forms an annular sheet along the post. Their impingement produces a finely atomized spray^[11]. It can be in general used in a liquid-liquid or gas-liquid configuration.

The primary design parameter is the Total Momentum Ratio (TMR), defined as the ratio of radial to axial stream momentum:

$$\text{TMR} = \frac{\dot{m}_r u_r}{\dot{m}_a u_a} \quad (1)$$

where \dot{m} is the mass flow rate, u the discharge velocity and the subscripts r and a stand respectively for radial and axial flows. The experimental tests show in general that the cone angle formed by the propellant spray increases with TMR^[11]. In the case of discrete orifices, the Local Momentum Ratio (LMR) is often employed^[9]:

$$\text{LMR} = \frac{\dot{m}_r u_r}{\frac{d}{w} \dot{m}_a u_a} \quad (2)$$

where d is the diameter of jet orifices, while w is the corresponding stream width of the jet orifice (see Fig.4). Thus, the LMR denominator corresponds to the momentum of the axial film segment that interacts with the associated radial jet. The spray angle can be correlated to LMR^[10]:

$$\theta = \arccos\left(\frac{1}{1 + \text{LMR}}\right) \quad (3)$$

Another key design parameter is the blockage factor (BF), defined as the ratio of the total circumferential length of the holes or slots to the circumference of the pintle^[11]:

$$\text{BF} = \frac{Nd}{\pi d_p} \quad (4)$$

where d_p is the pintle post diameter and N the number of orifices.

Finally, the skip distance is defined as the ratio of skip length (L_s) to pintle post diameter d_p , where the skip length is the length that the annular flow must travel before impacting the radial holes or gap. A smaller ratio leads to impingement and combustion near the chamber wall, risking overheating, while a larger ratio reduces collision intensity due to annular flow deceleration along the pintle post, degrading atomization efficiency. In general, larger skip distances lead to wider spray angles due to friction-induced changes in velocity profiles interacting with the jet^[11].

3. Modeling of discrete orifices gas-liquid pintle injectors

As stated in the Introduction, this work focuses on the case of discrete orifice gas-liquid pintle injectors. The motivation lies in the objective of verifying the validity of the Lagrangian approach with modeled primary breakup, in terms of consistency with the macroscopic characteristics of the spray (such as spray angle and characteristic diameters), as well as the spray pattern's response to different parameters, including L_s and LMR. The results of this work will act as a foundation for future work, which will focus on the annular gap pintle injector. Its underlying physics will be investigated in a similar manner, with the aim of identifying all characteristic parameters and ultimately producing a Rosin-Rammler diameter distribution along with corresponding velocity and angle profiles.

In a discrete orifice gas-liquid pintle injector, the liquid is injected as a jet that breaks up into droplets. As shown in Fig. 1, the atomization process is characterized by three distinct flow regimes – single-phase, cavitating, and flipped – with abrupt transitions that markedly affect spray behavior^[12]. These regimes govern the liquid exit velocity, initial droplet size, and dispersion angle.

A version of the plain orifice injector model is developed. In this model, the nozzle internal state is determined using the same decision tree of Ansys Fluent in Fig.2^[14].

The key parameter is the cavitation parameter K defined as^{[15],[16]}:

$$K = \frac{p_1 - p_v}{p_1 - p_2} \quad (5)$$

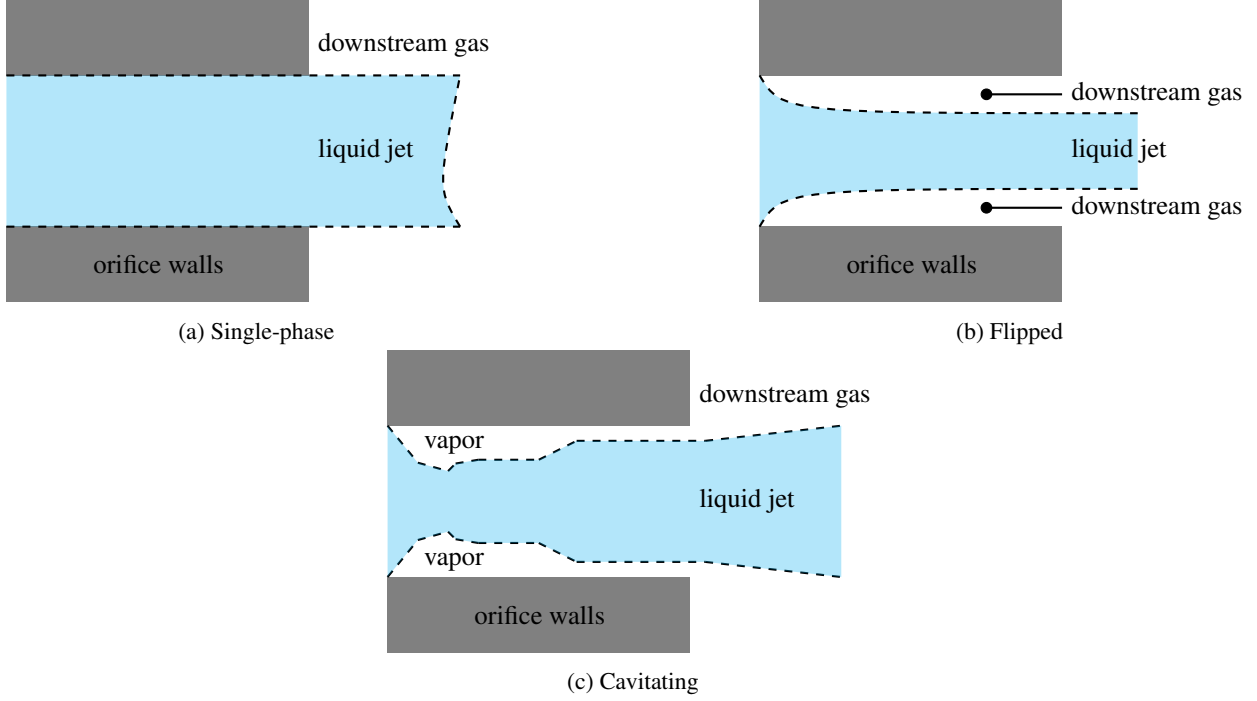


Figure 1: Discrete orifice operating modes^[13], adapted from Fluent manual^[14].

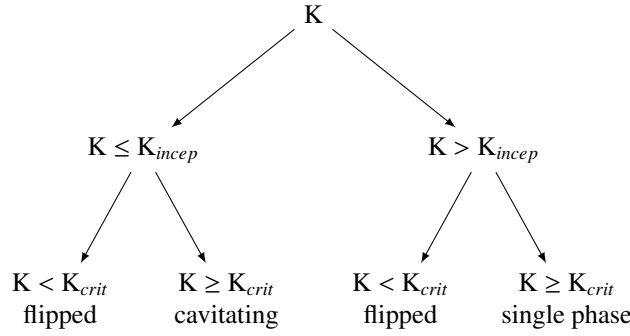


Figure 2: Decision tree for the state of the plain orifice nozzle.

where p_1 is the upstream pressure, p_2 is the downstream pressure and p_v is the vapor pressure at the liquid jet temperature. The parameter K is evaluated against the critical cavitation inception value K_{incep} . An empirical relation is employed for this comparison:

$$K_{incep} = 1.9 \left(1 - \frac{r_i}{d}\right)^2 - \frac{1000}{Re_h} \quad (6)$$

where r_i is the radius of the inlet corner, d is the orifice diameter and Re_h is the hydraulic Reynolds diameter defined as:

$$Re_h = \frac{d\rho_1}{\mu} \sqrt{\frac{2(p_1 - p_2)}{\rho_1}} \quad (7)$$

Using the same approach, the critical value of flip inception K_{crit} can be defined:

$$K_{crit} = 1 + \frac{1}{\left(1 + \frac{L}{4d}\right)\left(1 + \frac{2000}{Re_h}\right)e^{70r_i/d}} \quad (8)$$

where ρ_1 and μ are respectively the density and the viscosity of the fluid.

Before moving on, it is necessary to introduce some other definition. The coefficient of discharge is defined as

PINTLE INJECTOR SPRAY STUDY

the ratio of the mass flow rate through the nozzle to the theoretical maximum mass flow rate:

$$C_D = \frac{\dot{m}}{A \sqrt{2\rho_1(p_1 - p_2)}} \quad (9)$$

In the case of flipped or cavitating nozzle, a coefficient of contraction C_c is used to represent the reduction in the cross-sectional area of the liquid jet with the formulation by Nurick^[17]:

$$(C_c)_{r/d} = \left(\frac{1}{(C_{ct})_{r/d=0}^2} - \frac{11.4r_i}{d} \right)^{-0.5} \quad (10)$$

with $(C_{ct})_{r/d=0}$ which is a theoretical constant for flipped nozzles equal to 0.62.

3.1 Single phase

In the case of single-phase nozzles, Nurick's theory has been further extended to account for the effect of lower L/d ratios, where L is the orifice length and d its nominal diameter. The formula of the discharge coefficient by Lichtarowicz is^[18]:

$$C_d = \left(\frac{1}{C_{du}} + \frac{20}{Re_h} (1 + 2.25L/d) \right)^{-1} \quad (11)$$

where C_{du} is the ultimate discharge coefficient, valid for an asymptotic Reynolds number $Re > 2 \cdot 10^4$ and corrected for lower values with the previous equations, which can be expressed as:

$$C_{du} = 0.827 - 0.0085L/d \quad (12)$$

However, Eq.12 holds for $2 < L < 10$. In the case of pintle injectors with discrete orifices, as the conduit length corresponds solely to the thickness of the pintle, it is possible to see a L/d ratios below 2, which is the lower limit of the validity range of the above formula.

In order to extend the validation for lower L/d ratios, a polynomial fit was performed on the experimental data from Ref.^[18], imposing continuity constraints on both the function value and its derivative at the point $L/d = 2$. Specifically, the fitted function was determined such that for $2 < L/d < 10$ it smoothly connects, in both value and slope, with the previously established formula in Eq.12. The target value and derivative at the matching point were set as:

$$C_{du}(2) = 0.827 - 0.0085 \cdot 2 \quad C'_{du}(2) = \frac{dC_{du}}{d(L/d)}(2) = -0.0085. \quad (13)$$

The fit was obtained by minimizing the sum of squared residuals between the polynomial and the experimental data, subject to the above constraints. The optimization was performed using the `fmincon` Matlab function, starting from an initial guess provided by an unconstrained polynomial fit. This approach ensures continuity of the overall model, avoiding discontinuities in both value and slope between the two expressions in their respective validity ranges. The results can be seen in Fig.7a. By applying the Eq. 12 using as C_{du} the output of the fit calculated for $L/d = 1$, it is possible to see a good agreement with the experimental results of James^[18].

The exit velocity is then found from the conservation of mass and the assumption of a uniform exit velocity. It is possible to find the spray angle using the formula from Ranz^[19]:

$$\frac{\theta}{2} = \tan^{-1} \left[\frac{4\pi}{C_A} \sqrt{\frac{\rho_g}{\rho_l}} \sqrt{\frac{\sqrt{3}}{6}} \right] \quad (14)$$

where the gas density ρ_g appears and the parameter C_A can be found using the correlation from Reitz^[20] and is related to the injector geometry:

$$C_A = 3 + \frac{L}{3.6d} \quad (15)$$

Finally, the two parameters of Rosin-Rammler distribution are found, namely the most probable diameter d_0 and the spread parameter s . For flows through single-phase nozzles, the empirical relation proposed by Wu^[21] is applied:

$$d_{32} = 133\lambda We^{-0.74} \quad (16)$$

where d_{32} is the Sauter Mean Diameter (SMD). Here, $\lambda = d/8$ represents the radial integral length scale at the exit of the nozzle for a fully developed turbulent pipe flow, and We denotes the Weber number, defined as:

$$We = \frac{\rho_1 u^2 \lambda}{\sigma} \quad (17)$$

where σ is the surface tension of the liquid droplets. The spread parameter is found from experimental observations and is set to $s = 3.5$ for a single phase nozzle^{[14],[16]}. Finally, Lefevbre's correlation^[16] relates d_0 the SMD d_{32} to the most probable diameter of the Rosin-Rammler distribution:

$$d_0 = 1.2726d_{32} \left(1 - \frac{1}{s}\right)^{1/s} \quad (18)$$

3.2 Cavitating

In the case of cavitating nozzle, the theory of Nurick is applied^[15]. The coefficient of discharge can be found using directly the contraction coefficient of Eq.10 and the cavitation parameter from Eq.5:

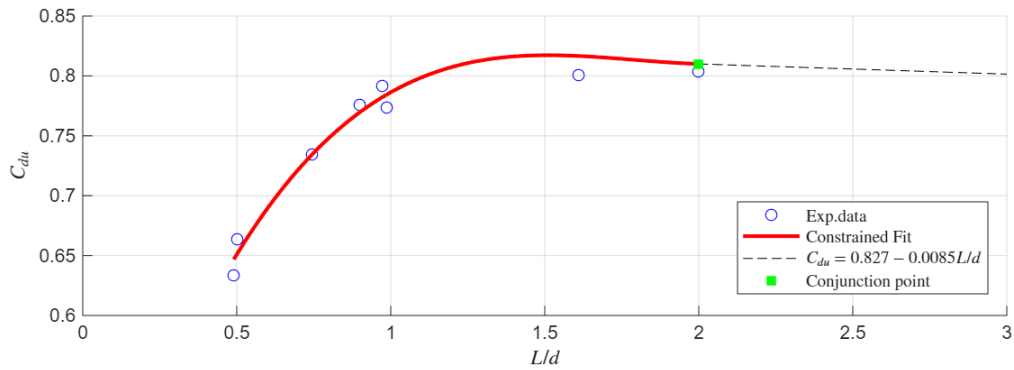
$$C_d = C_c \sqrt{K} \quad (19)$$

For more details on the derivation of the formula, the reader is referred to Nurick's work^[15].

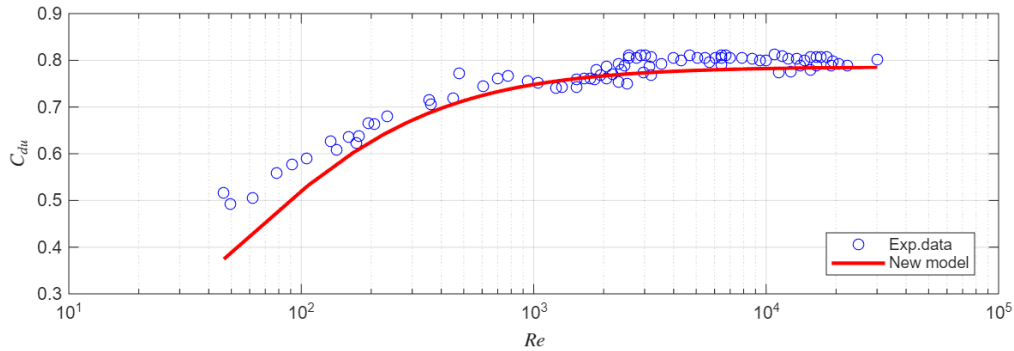
For the exit velocity and effective area, the formulations of Schmidt^[22] is used:

$$V_{\text{eff}} = \frac{(2C_c p_1 - p_2 + (1 - 2C_c)p_v)}{C_c \sqrt{2\rho(p_1 - p_v)}} \quad (20)$$

$$A_{\text{eff}} = \frac{2C_c^2(p_1 - p_v)}{(2C_c p_1 - p_2 + (1 - 2C_c)p_v)} A \quad (21)$$



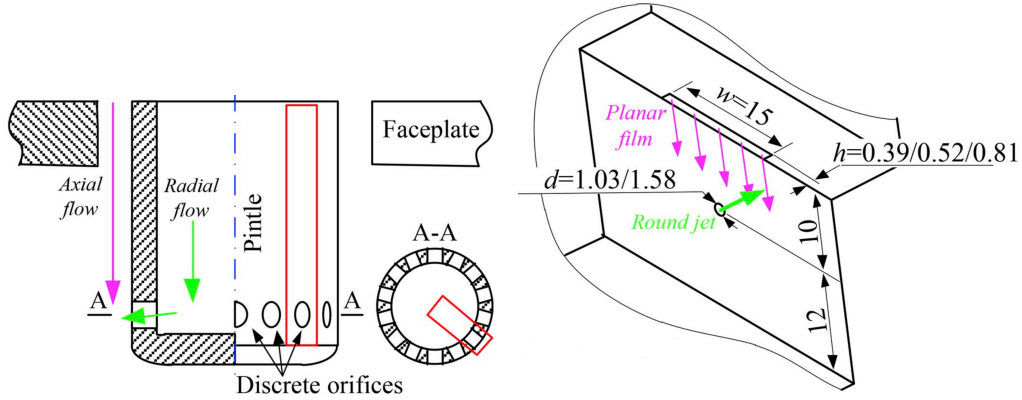
(a) Fit of the experimental data



(b) Results for $L/d = 1$

Figure 3: Results of the model for lower L/d ratios.

PINTLE INJECTOR SPRAY STUDY



(a) Schematic of the pintle injector with discrete orifices. (b) Configuration and dimensions of the pintle injector element.

Figure 4: Testcase pintle injector^[10].

where A is the original injector exit area. The exit angle is the same of the single phase case. The effective diameter computed from area is then used in the calculation of the radial integral length scale at the exit of the nozzle and the SMD with Eq.16, and it is used to find the most probable diameter^[16]:

$$d_0 = 2.76015d_{32} \left(1 - \frac{1}{s}\right)^{1/s} \quad (22)$$

In this case, the spread parameter is set to $s = 1.5$ ^[14].

3.3 Flip condition

In the hydraulic flip condition, the discharge coefficient is set to its theoretical value from the potential flow analysis ($C_{ct})_{r/d=0} = 0.62$, while the exit velocity is found from the conservation of mass and the value of the reduced flow area calculated from C_{ct} . The exit angle is set to a small arbitrary value (in this case 0.01rad)^[14] and the most probable diameter is considered equal to the liquid jet's one. The spread parameter is set to $s = \infty$, which means that the distribution becomes monodisperse, with all particles having exactly the same diameter and no size variation.

4. CFD simulations

A series of CFD simulations using the software Ansys Fluent is performed in order to compare the result with an experimental testcase^[10] and to create an appropriate database for the GAN training.

4.1 Testcase description

The pintle injectors with discrete orifices are simplified into a pintle injector element: in fact, the inner flow of the sprays was hard to observe due to obstruction by the outer sprays. To address this, a specific injector element was selected, and the annular film was simplified to a planar form. Fig.4 shows the injector's layout and key dimensions. The film thicknesses used were 0.39 mm, 0.52 mm, and 0.81 mm, with jet diameters of 1.03 mm and 1.58 mm. In our simulations, just the film thickness of 0.81 mm is considered.

4.2 Numerical modeling

The problem of the liquid injection in crossflow is addressed using an Euler-Lagrangian approach^[14], where the gas phase is treated as a continuum by solving the Navier-Stokes equations, and the dispersed phase is modeled by tracking numerous droplets through the resulting flow field. The two phases can exchange momentum, mass, and energy.

4.2.1 Gas phase governing equations

Continuity:

$$\frac{\partial \rho}{\partial t} + \nabla \cdot (\rho \vec{v}) = S_m \quad (23)$$

Momentum:

$$\frac{\partial(\rho \vec{v})}{\partial t} + \nabla \cdot (\rho \vec{v} \vec{v}) = -\nabla p + \nabla \cdot (\bar{\tau}) + \rho \vec{g} + \vec{F} \quad (24)$$

Energy:

$$\frac{\partial(\rho E)}{\partial t} + \nabla \cdot (\vec{v}(p + \rho E)) = \nabla \cdot (k_{\text{eff}} \nabla T + (\bar{\tau}_{\text{eff}} \cdot \vec{v})) \quad (25)$$

4.2.2 Liquid phase

The motion of a discrete phase particle is calculated by integrating the force balance acting on it, expressed in a Lagrangian reference frame^[14]:

$$m_p \frac{d\vec{u}_p}{dt} = m_p \frac{\vec{v} - \vec{u}_p}{\tau_r} + m_p \frac{\vec{g}(\rho_p - \rho)}{\rho_p} + \vec{F}_e \quad (26)$$

where the drag force $m_p \frac{\vec{v} - \vec{u}_p}{\tau_r}$ appears. The droplet relaxation time τ_r is written as^[23]:

$$\tau_r = \frac{\rho_p d_p^2}{18\mu} \frac{24}{C_d Re} \quad (27)$$

where the relative Reynolds number is:

$$Re = \frac{\rho d_p |\vec{u}_p - \vec{v}|}{\mu} \quad (28)$$

By integrating Eq.26 with respect to time, the particle's velocity is obtained at each location along its path, and the trajectory is subsequently determined by:

$$\frac{d\vec{x}}{dt} = \vec{u}_p \quad (29)$$

Simulating every droplet in a spray is computationally intensive, so droplets with similar size and velocity are grouped into parcels. Each parcel represents many real droplets, offering an efficient and statistically reliable way to model the spray. This method is effective when a sufficient number of parcels is used to accurately represent the spray's statistical behavior.

4.2.3 Drag law

Drag is a key factor in Lagrangian particle tracking, as it strongly influences particle motion. Accurate drag coefficient estimation is therefore critical for reliable spray modeling.

In this study, the drag coefficient C_d in Eq. 27 is estimated using the dynamic drag law^[14], known for its robustness in such applications. While particles are often assumed to be spherical, high Weber numbers can cause droplet deformation, sometimes into disk-like shapes. Since disks experience higher drag than spheres, the dynamic model accounts for this by linearly adjusting from the spherical value up to 1.54, representing a disk. The model is expressed as^[24]:

$$C_d = C_{d,\text{sphere}}(1 + 2.632y) \quad (30)$$

where:

$$C_{d,\text{sphere}} = \begin{cases} 0.424 & \text{Re} > 1000 \\ \frac{24}{\text{Re}} \left(1 + \frac{\text{Re}^{2/3}}{6}\right) & \text{Re} \leq 1000 \end{cases} \quad (31)$$

and y is the droplet distortion determined by the solution of the following equation:

$$\frac{d^2 y}{dt^2} = \frac{C_F \rho_g u^2}{C_b \rho_l r_d^2} - \frac{C_k \sigma}{\rho_l r^3} y - \frac{C_d \mu_l}{\rho_l r^2} \frac{dy}{dt} \quad (32)$$

This equation is tied to the TAB model for spray breakup. When $y = 0$ the droplet is spherical; at $y = 1$ it represents a disk.

4.2.4 Breakup model

Accurate modeling of spray breakup is crucial for achieving reliable results. Several models, each valid within specific application ranges, have been proposed in the literature. In this work, the Schmehl Breakup Model is employed because of its accuracy in subsonic crossflows. The Schmehl model^[25] distinguishes between three breakup regimes: Bag Breakup, Multimode Breakup, and Shear Breakup. The regime in which a droplet falls is determined based on the Weber number, which quantifies the strength of aerodynamic forces relative to surface tension, and the Ohnesorge number, which characterizes the damping effect of viscous forces relative to surface tension.

4.2.5 Turbulence modeling

The Reynolds-Averaged Navier-Stokes (RANS) equations were used together with the Menter SST (Shear-Stress Transport) model^[26], which has proven reliable for various crossflow injection scenarios^[13].

4.2.6 Numerical setup

The computational domain has been created in order to reproduce the domain, also by following the indication of the experimental testcase authors^[27]. The injector nozzle has been placed at the midpoint of the base and 10 mm away from the inlet. Given the experimental conditions, the boundary conditions set can be found in Table 1.

After a convergence study, a grid of approximately 80,000 cells was chosen. The difference on the spray angle between a 320,000 cell configuration was around 0.8° . The value are in line with other numerical tests from the author. However, a maximum $y+$ value of 11 can be found on the wall: further work will include the use of more refined meshes.

The simulation employed a pressure-based solver with *SIMPLE* pressure-velocity treatment. To ensure numerical stability, a steady-state analysis was first conducted to initialize the flow fields with undisturbed conditions. Following initialization, a transient simulation was carried out to capture the dynamics of water injection into the crossflow, with a first-order implicit scheme used for time integration. For spatial discretization, a second-order upwind scheme was applied to all transport equations. The timestep was chosen as $1e - 05$ s after an appropriate convergence study.

4.3 Database creation

A tailored simulation matrix was constructed, from which snapshots at different time instances were extracted to be used for training the GAN. The simulations were carried out with crossflow velocities ranging from 30 to 50 m/s, consistent with the typical operating conditions for this class of injectors^[1]. Two injector diameters were considered: 1.03 mm and 1.58 mm. The water mass flow rates and corresponding injection velocities, serving as input parameters to the model, were determined to yield LMR values within the range 0-2, which is of primary interest for practical applications.

Following the simulations, a verification step was performed by comparing the actual flow rates and velocities obtained from the CFD outputs for both air and water. This comparison confirmed a good agreement between the target LMR values and those computed from the simulation results.

The training database for the GAN consists of only 85 snapshots corresponding to different time instants taken from the performed simulations. The future goal is precisely to achieve meaningful results using only a few snapshots, thanks to conditioning techniques based on the physical knowledge of the problem.

Boundary Condition	Description
Velocity Inlet	$p = 101325$ Pa $u_\infty = 50$ m/s $T = 300$ K
Pressure Outlet	$p = 101325$ Pa Backflow $T_o = 300$ K
Wall	Adiabatic wall

Table 1: Boundary conditions.

LMR	0.3012	0.2934	0.1878	0.1304	0.1177	1.8826	1.0590	0.6777	0.2306	1.3074	5.2295
θ [deg]	46.33	46.04	41.15	37.94	37.03	75.53	64.20	57.58	43.72	68.23	81.85

Table 2: LMR values and corresponding expected angles θ (in degrees), computed as $\theta = \arccos\left(\frac{1}{1+LMR}\right)$

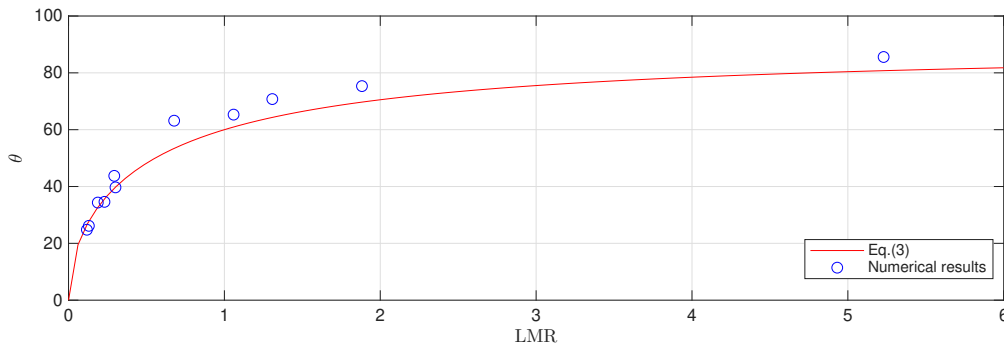


Figure 5: Results of the CFD simulations

4.4 Results

The results are summarized in Fig.5. The trend is as expected, although a slight overestimation of the spray angle can be observed for larger LMR values. The issues are likely related to the mesh size and the time step: at this stage, the focus was on obtaining preliminary results at very low computational cost (2 hours using 18 physical cores per simulation). Future work will aim at improving the model and investigating ad-hoc droplet breakup models. Nevertheless, even at this stage, the particle diameters—particularly the Sauter Mean Diameter (SMD)—are in line with the expected values for this type of flow, typically on the order of tens of micrometers. This is further confirmed by the spray angle trend, which naturally depends on the particle size and thus on the droplet diameter itself. The pressure and velocity fields, omitted here for the sake of brevity, are consistent with expectations, and the underlying physics, such as the presence of the Counter-Rotating Vortex Pair (CVP), is accurately captured.

5. Generative Adversarial Network (GAN) for spray field generation

5.1 Convolutional Neural Networks and Generative Adversarial Framework

Convolutional Neural Networks (CNNs) are a widely adopted class of deep learning models, particularly effective for processing grid-structured data such as images. Their architecture is based on convolutional layers that apply shared kernel filters across the input space, enabling the extraction of local and hierarchical spatial features. In this work, CNNs serve as the foundational architecture for both the generator and the discriminator within a Generative Adversarial Network (GAN), due to their ability to efficiently model spatial dependencies and preserve geometric structures, an essential property for the generation of physically plausible spray patterns.

Generative Adversarial Networks (GANs), first introduced by Goodfellow et al.^[28], provide a powerful framework for learning complex data distributions through adversarial training. A GAN consists of two neural networks, a generator G and a discriminator D , that are trained simultaneously in a two-player minimax game. The generator $G(z)$, given a latent vector $z \sim p_z(z)$, produces synthetic data samples intended to resemble those from the true data distribution p_{data} . The discriminator $D(x)$ attempts to distinguish between real samples $x \sim p_{data}(x)$ and those generated by G .

The training objective is formalized as:

$$\min_G \max_D \mathbb{E}_{x \sim p_{data}(x)} [\log D(x)] + \mathbb{E}_{z \sim p_z(z)} [\log(1 - D(G(z)))] \quad (33)$$

where \mathbb{E} is the expectation operator (or expected value). This adversarial loss drives the generator to produce increasingly realistic samples that can deceive the discriminator. In practical implementations, modified loss functions are often employed to address issues such as vanishing gradients and training instability. For instance, using the non-saturating loss for the generator:

$$\min_G \mathbb{E}_{z \sim p_z(z)} [-\log D(G(z))] \quad (34)$$

can significantly improve convergence by providing stronger gradients early in training.

The generator network is constructed using a sequence of transposed convolutional layers, which iteratively upsample the latent representation into a high-resolution image. To enhance training stability and facilitate effective gradient propagation, each layer is followed by batch normalization and LeakyReLU activations. Conversely, the discriminator comprises conventional convolutional layers, which downsample the input image while capturing discrimi-

PINTLE INJECTOR SPRAY STUDY

native features. These are subsequently integrated with encoded physical parameters to enable the binary classification of images as real or synthetic.

In this study, we leverage conditional GANs (cGANs) to synthesize spray pattern images from specified physical parameters. By incorporating these parameters into both the generator and discriminator pathways, the model learns to produce images that are not only realistic but also physically consistent with the input conditions. The use of CNN-based architectures ensures that spatial features of the spray, such as symmetry and dispersion, are effectively preserved throughout the generative process.

It is emphasized that in this work, GANs are employed to generate instantaneous fields corresponding to operating conditions already included in the database; however, this represents only a preliminary step toward the ultimate objective of leveraging GANs for the predictive generation of snapshots under unseen operating conditions.

5.2 Physics-Based Conditioning

In our implementation, we condition the image generation process on both physical parameters (LMR, m) and the expected spray angle θ . This is achieved by extending the input vector to the generator with a normalized version of θ (i.e., $\theta/90$). These inputs are first encoded via fully connected layers before being concatenated with the latent noise vector.

During training, a custom physics-informed loss term is added to the generator’s objective to explicitly enforce physical consistency:

$$\mathcal{L}_{phys} = |\theta_{gen} - \theta_{target}|$$

Here, θ_{gen} is computed from the generated image using an image-processing-based estimation algorithm (described in the next section), and θ_{target} is the known conditioning angle from Eq.3. This term is weighted and added to the adversarial loss to guide the generator not only toward realism but also toward adherence to domain-specific expectations. This approach enables the model to integrate physical interpretability directly into the image synthesis process.

5.3 Spray Angle Estimation

The developed algorithm for image-processing-based spray angle estimation can be seen in Fig.6. The spray angle estimation algorithm employs a multi-stage image processing approach to quantify the geometric characteristics of liquid spray patterns. Initially, the input image undergoes preprocessing through grayscale conversion and Gaussian blur filtering (5x5 kernel) to reduce noise artifacts. The spray region is subsequently identified using intensity-based thresholding, where pixels exceeding a configurable threshold are classified as spray particles. Morphological opening and closing operations with a 3x3 kernel are applied to eliminate small noise components and fill gaps in the detected spray region. The algorithm then extracts the lower boundary of the spray by sampling at regular intervals (every 3 pixels) across the spray width and identifying the maximum y-coordinate at each x-position, effectively capturing the spray envelope. To ensure robust angle calculation, the method allows for selective point filtering within a specified distance range, enabling analysis of specific spray regions while excluding near-field or far-field disturbances. A linear regression model is fitted to the selected boundary points using least-squares method, and the spray half-angle is calculated as the arctangent of the absolute slope of the fitted line relative to the horizontal axis.

5.4 Results

The results after 2000 training epochs are shown in Fig.7. It can be observed that the prediction aligns well with the original images, despite the low number of neural network parameters, the use of a noise vector with only 2 components, and just 2000 training epochs. The spray pattern is consistent with the instantaneous fields, and the particle sizes (indicated here by the colors) exhibit a spatial structure that conforms to the original, albeit with reduced definition and fewer features. An interesting phenomenon is the slight improvement in the spray angle for high LMR configurations, which previously showed a relatively high error. Further investigation is needed to determine whether this effect is due to the low resolution, limited number of features, or short training time, or whether it is a consequence of the physical conditioning. As expected, the predictive capability is reliable only for operating conditions already represented in the training dataset. The primary goal remains to enhance the physical conditioning by introducing new techniques that reduce the need for excessively large training datasets.

6. Conclusions and further works

In this study, a numerical model of a discrete orifice pintle injector was developed, specifically optimized for configurations with low length-to-diameter (L/d) ratios. Computational Fluid Dynamics (CFD) simulations showed good agreement with experimental data and delivered physically consistent outcomes, thereby validating both the Lagrangian injection method and the chosen breakup model. The resulting set of simulations was used to train a physics-conditioned Generative Adversarial Network (GAN), based on Convolutional Neural Networks (CNNs) and coupled with a real-time spray evaluation module. The introduction of a physics-based loss term enhanced the training performance. Preliminary results exhibit promising behavior, despite the limited expressiveness of the images due to the deliberately lightweight and computationally efficient model.

Future work will focus on the following directions:

- Improving the current model by integrating Volume of Fluid (VOF) techniques to better capture phenomena such as flip and cavitation, particularly in relation to internal geometries and multi-row pintle injector configurations.
- Expanding the framework to include continuous gap pintle injectors, along with the implementation and validation of breakup models suitable for liquid sheet disintegration.
- Testing the predictive capability of GANs in generating spray fields under operating conditions not included in the training database.
- Investigating alternative GAN architectures, such as U-Net-based generators, and exploring new types of physics-informed conditioning to refine the loss function and broaden the model's predictive scope beyond the original training set.

7. Acknowledgements

This work was supported by the Italian Ministry of University and Research (MIUR) under the PRIN 2022 research project *NextGenSProDesT - Next Generation Space Propulsion Design Techniques*. The authors gratefully acknowledge this support.

References

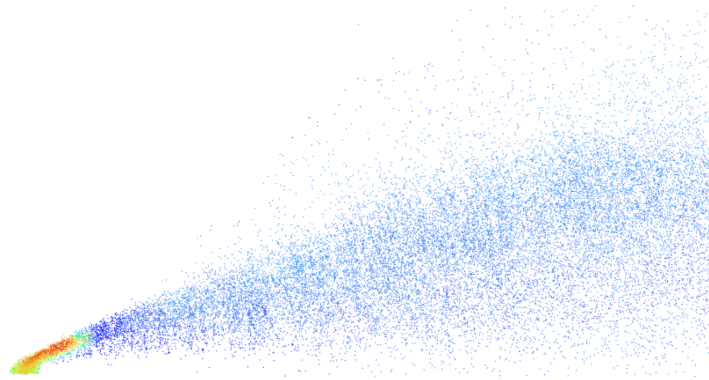
- [1] N. Ashgriz. *Handbook of Atomization and Sprays: Theory and Applications*. SpringerLink : Bücher. Springer US, 2011. ISBN: 9781441972644. URL: <https://books.google.it/books?id=ARKo1wxcdgQC>.
- [2] Jacopo Liberatori et al. "Injection of LOX spray in Methane cross-flow RANS modeling uncertainty quantification". In: *AIAA Propulsion and Energy 2021 Forum*. DOI: 10.2514/6.2021-3570. URL: <https://arc.aiaa.org/doi/abs/10.2514/6.2021-3570>.
- [3] L. Lucchese et al. "Impact of chemical modeling on the numerical analysis of a LOx/GCH4 rocket engine pintle injector". In: *Acta Astronautica* 218 (2024), pp. 240–250. ISSN: 0094-5765. DOI: 10.1016/j.actaastro.2024.02.038. URL: <https://www.sciencedirect.com/science/article/pii/S0094576524001103>.
- [4] Leandro Lucchese et al. "Sensitivity Analysis of a Continuous-Slit Pintle Injector to the Chemical Kinetics Modeling". In: *AIAA SCITECH 2025 Forum*. DOI: 10.2514/6.2025-1548. eprint: <https://arc.aiaa.org/doi/pdf/10.2514/6.2025-1548>. URL: <https://arc.aiaa.org/doi/abs/10.2514/6.2025-1548>.
- [5] Francis H. Harlow and J. Eddie Welch. "Numerical Calculation of Time-Dependent Viscous Incompressible Flow of Fluid with Free Surface". In: *The Physics of Fluids* 8.12 (Dec. 1965), pp. 2182–2189. ISSN: 0031-9171. DOI: 10.1063/1.1761178. eprint: https://pubs.aip.org/aip/pfl/article-pdf/8/12/2182/12731401/2182_1_online.pdf. URL: <https://doi.org/10.1063/1.1761178>.
- [6] C. W. Hirt and B. D. Nichols. "Volume of fluid (VOF) method for the dynamics of free boundaries". In: *Journal of Computational Physics* 39.1 (1981), pp. 201–225. ISSN: 0021-9991. DOI: 10.1016/0021-9991(81)90145-5. URL: <https://www.sciencedirect.com/science/article/pii/0021999181901455>.
- [7] Justin J. Nijdam et al. "Lagrangian and Eulerian models for simulating turbulent dispersion and coalescence of droplets within a spray". In: *Applied Mathematical Modelling* 30.11 (2006). Selected papers from the Third International Conference on CFD in the Minerals and Process Industries, pp. 1196–1211. ISSN: 0307-904X. DOI: <https://doi.org/10.1016/j.apm.2006.02.001>. URL: <https://www.sciencedirect.com/science/article/pii/S0307904X06000217>.

PINTLE INJECTOR SPRAY STUDY

- [8] Hao Ma et al. “Generative adversarial networks with physical evaluators for spray simulation of pintle injector”. In: *AIP Advances* 11.7 (July 2021), p. 075007. ISSN: 2158-3226. DOI: 10.1063/5.0056549. eprint: https://pubs.aip.org/aip/adv/article-pdf/doi/10.1063/5.0056549/12843691/075007\1_online.pdf. URL: <https://doi.org/10.1063/5.0056549>.
- [9] Fan Zhao et al. “Review of atomization and mixing characteristics of pintle injectors”. In: *Acta Astronautica* 200 (2022), pp. 400–419. ISSN: 0094-5765. DOI: <https://doi.org/10.1016/j.actaastro.2022.08.042>. URL: <https://www.sciencedirect.com/science/article/pii/S0094576522004556>.
- [10] Peng Cheng, Qinglian Li, and Huiyuan Chen. “Flow characteristics of a pintle injector element”. In: *Acta Astronautica* 154 (2019), pp. 61–66. ISSN: 0094-5765. DOI: <https://doi.org/10.1016/j.actaastro.2018.10.020>. URL: <https://www.sciencedirect.com/science/article/pii/S0094576518309883>.
- [11] Suji Lee, Jaye Koo, and Youngbin Yoon. “Effects of skip distance on the spray characteristics of a pintle injector”. In: *Acta Astronautica* 178 (2021), pp. 471–480. ISSN: 0094-5765. DOI: <https://doi.org/10.1016/j.actaastro.2020.09.043>. URL: <https://www.sciencedirect.com/science/article/pii/S0094576520305853>.
- [12] Celia Soteriou, Richard Andrews, and Mark T. Smith. “Direct Injection Diesel Sprays and the Effect of Cavitation and Hydraulic Flip on Atomization”. In: *SAE transactions* 104 (1995), pp. 128–153. URL: <https://api.semanticscholar.org/CorpusID:135758469>.
- [13] Leonardo Stumpo et al. “Preliminary Validation and Sensitivity Analysis on a Eulerian/Lagrangian RANS Approach for Liquid Injection in Supersonic Crossflow”. In: *AIAA SCITECH 2025 Forum*. 2025. DOI: 10.2514/6.2025-1882. eprint: <https://arc.aiaa.org/doi/pdf/10.2514/6.2025-1882>. URL: <https://arc.aiaa.org/doi/abs/10.2514/6.2025-1882>.
- [14] ANSYS Inc. *ANSYS Fluent Theory Guide*. Release 2023R1. ANSYS Inc. 2023.
- [15] W. H. Nurick. “Orifice Cavitation and Its Effect on Spray Mixing”. In: *Journal of Fluids Engineering* 98.4 (1976), pp. 681–687. ISSN: 0098-2202. DOI: 10.1115/1.3448452. eprint: https://asmedigitalcollection.asme.org/fluidsengineering/article-pdf/98/4/681/5702170/681_1.pdf. URL: <https://doi.org/10.1115/1.3448452>.
- [16] A. H. Lefebvre and V. G. McDonell. *Atomization and Sprays*. CRC Press, 2017. ISBN: 9781498736268. URL: <https://books.google.it/books?id=80OEDgAAQBAJ>.
- [17] W. H. Nurick. “Orifice Cavitation and Its Effect on Spray Mixing”. In: *Journal of Fluids Engineering* 98.4 (Dec. 1976), pp. 681–687. ISSN: 0098-2202. DOI: 10.1115/1.3448452. eprint: <https://asmedigitalcollection.asme.org/fluidsengineering/article-pdf/98/4/681/5702170/681\1.pdf>. URL: <https://doi.org/10.1115/1.3448452>.
- [18] A. Lichtarowicz, R. K. Duggins, and E. Markland. “Discharge Coefficients for Incompressible Non-Cavitating Flow through Long Orifices”. In: *Journal of Mechanical Engineering Science* 7.2 (1965), pp. 210–219. DOI: 10.1243/JMES_JOUR_1965_007_029_02. eprint: https://doi.org/10.1243/JMES_JOUR_1965_007_029_02. URL: https://doi.org/10.1243/JMES_JOUR_1965_007_029_02.
- [19] William E. Ranz. “Some experiments on orifice sprays”. In: *The Canadian Journal of Chemical Engineering* 36.4 (1958), pp. 175–181. DOI: <https://doi.org/10.1002/cjce.5450360405>. eprint: <https://onlinelibrary.wiley.com/doi/pdf/10.1002/cjce.5450360405>. URL: <https://onlinelibrary.wiley.com/doi/abs/10.1002/cjce.5450360405>.
- [20] R. D. Reitz and F. V. Bracco. “Mechanism of atomization of a liquid jet”. In: *The Physics of Fluids* 25.10 (Oct. 1982), pp. 1730–1742. ISSN: 0031-9171. DOI: 10.1063/1.863650. eprint: https://pubs.aip.org/aip/pfl/article-pdf/25/10/1730/12414196/1730\1_online.pdf. URL: <https://doi.org/10.1063/1.863650>.
- [21] P.-K. Wu, L.-K. Tseng, and G. Faeth. “Primary breakup in gas/liquid mixing layers for turbulent liquids”. In: *30th Aerospace Sciences Meeting and Exhibit*. 1992. DOI: 10.2514/6.1992-462. eprint: <https://arc.aiaa.org/doi/pdf/10.2514/6.1992-462>. URL: <https://arc.aiaa.org/doi/abs/10.2514/6.1992-462>.
- [22] David P. Schmidt and Michael L. Corradini. “Analytical Prediction of the Exit Flow of Cavitating Orifices”. In: *Atomization and Sprays* 7.6 (1997), pp. 603–616. ISSN: 1044-5110.
- [23] Roy G. Gordon. “Error Bounds in Equilibrium Statistical Mechanics”. In: *Journal of Mathematical Physics* 9.5 (May 1968), pp. 655–663. ISSN: 0022-2488. DOI: 10.1063/1.1664624. eprint: https://pubs.aip.org/aip/jmp/article-pdf/9/5/655/19326157/655\1_online.pdf. URL: <https://doi.org/10.1063/1.1664624>.

- [24] Alex Liu, Daniel Mather, and Rolf Reitz. “Modeling the Effects of Drop Drag and Breakup on Fuel Sprays”. In: (Mar. 1993), p. 17. doi: 10.4271/930072.
- [25] R Schmehl et al. “Efficient numerical calculation of evaporating sprays in combustion chamber flows”. In: *92nd Symp. on Gas Turbine Combustion, Emissions and Alternative Fuels, RTO Meeting Proceedings*. Vol. 14. 1998.
- [26] F. R. Menter. “Two-equation eddy-viscosity turbulence models for engineering applications”. In: *AIAA Journal* 32.8 (1994), pp. 1598–1605. doi: 10.2514/3.12149. eprint: <https://doi.org/10.2514/3.12149>. url: <https://doi.org/10.2514/3.12149>.
- [27] Peng Cheng et al. “On the prediction of spray angle of liquid-liquid pintle injectors”. In: *Acta Astronautica* 138 (2017). The Fifth International Conference on Tethers in Space, pp. 145–151. issn: 0094-5765. doi: <https://doi.org/10.1016/j.actaastro.2017.05.037>. url: <https://www.sciencedirect.com/science/article/pii/S0094576517304782>.
- [28] Ian J. Goodfellow et al. *Generative Adversarial Networks*. 2014. arXiv: 1406.2661 [stat.ML]. url: <https://arxiv.org/abs/1406.2661>.

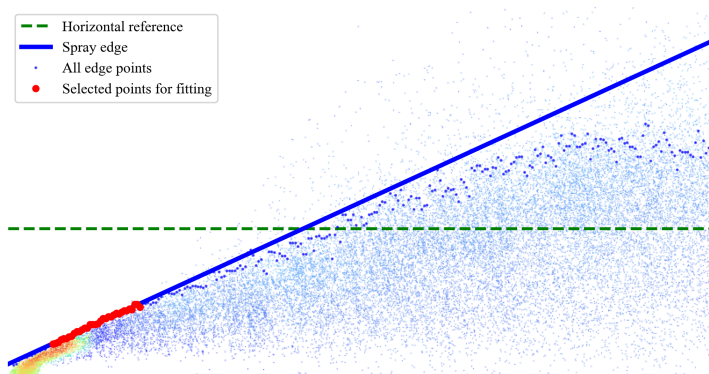
PINTLE INJECTOR SPRAY STUDY



(a) Original spray



(b) Filtered spray



(c) Angle estimation

Figure 6: Results of angle estimation algorithm.

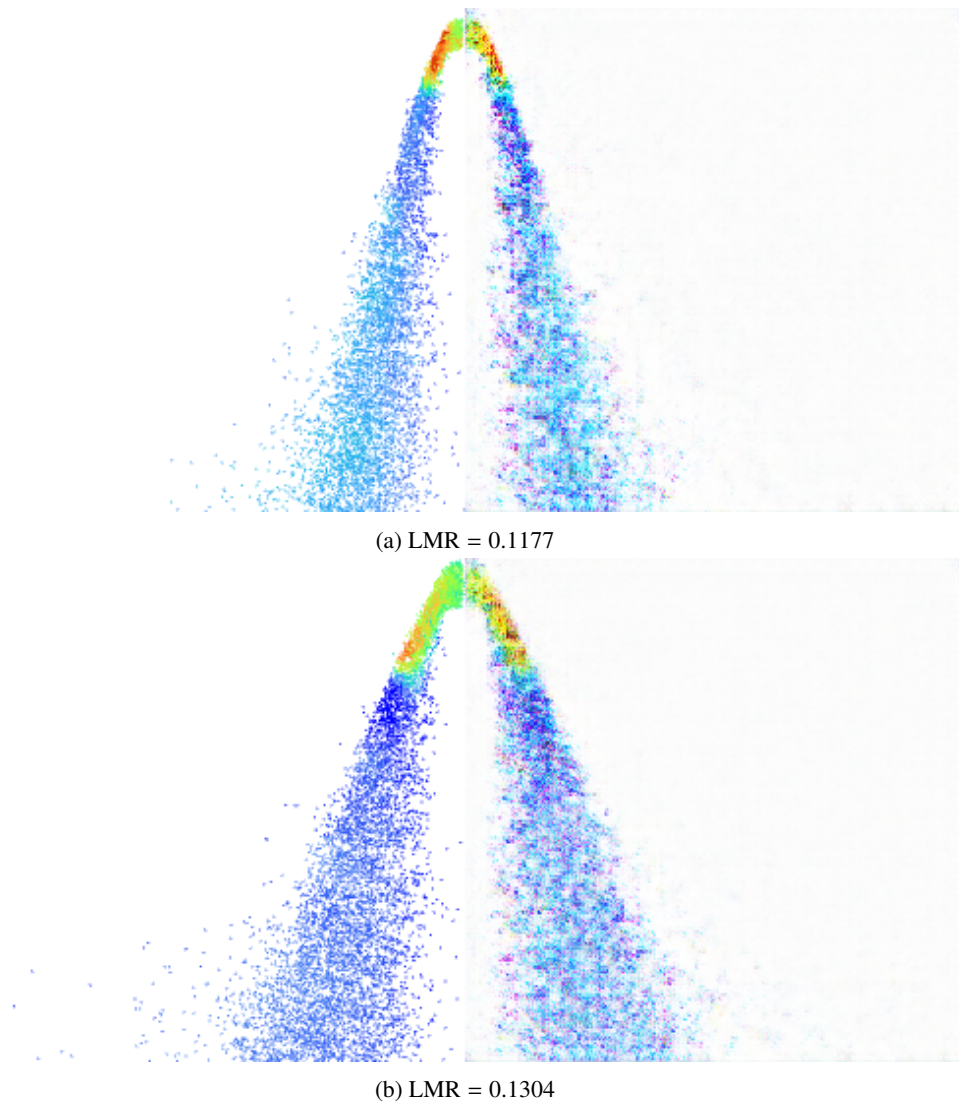


Figure 7: Results of the GAN training. Left: CFD simulation result; right: GAN-generated picture.